Detecting agglomeration patterns on solid propellant surface via a new curvature-based multiscale method

Thomas Geoffrey Decker, Robin William Devillers, Stany Gallier

Detecting agglomeration patterns on solid propellant surface via a new curvature-based multiscale method

Thomas Geoffrey Decker[a,*], Robin William Devillers[a], Stany Gallier[b]

[a]*DMPE, ONERA, Université Paris Saclay, Palaiseau, F-91123*
[b]*ArianeGroup, Le Bouchet Research Center, 91710 Vert le Petit, France*

Abstract

In this article, a new algorithm detecting particles and aggregates on the surface of a burning solid propellant containing inert particles is presented. Shadowgraphy images are captured using a set-up at ONERA. Four propellants containing particles of different sizes are used. Detecting the surface being well studied, the method rather focuses on detecting protrusions of a continuous 1D curve. Curvature is the basic tool used, it can be calculated using Gaussian filters of different widths. A normalization is proposed, ensuring curvatures of different filter widths to be compared, meaning the algorithm can detect protrusions of different sizes. The result is the Extreme of the Normalized Curvature (ENC), detecting concave parts of a curve, independently of the size of the protrusion. While the ENC detects the main concavities, the limits of the targeted patterns (convexities) are found by a multi-scale approach following the detection.

Evaluating the performances of the algorithm is possible thanks to the annotations of some images. Both detection performances and limit research performances are investigated. The influence of the initial particle size on the performances is studied.

Keywords: Solid propellant, Inert particles agglomeration, Image processing, Protrusion detection, Curvature, Gaussian filter

1. Introduction

Solid Rocket Motors (SRM) are widely used in spatial propulsion in both civilian and military applications. They produce a major thrust, have very few reliability issues and can be ignited at any moment. The fuel is a solid material named solid propellant. Most motors burn a composite solid propellant, which is composed of three main ingredients. The first is the oxidizer, classically Ammonium Perchlorate (AP) particles embedded in a polymer binder, classically Hydroxyl-Terminated PolyButadiene (HTPB). They react together when the solid propellant is ignited. Aluminum particles can also be added for better performance. The oxidizer and the polymer binder burn at the surface of the propellant, producing gas. The aluminum particles are ejected as the propellant burns and are ignited in the gas flow produced. While the propellant is consumed, the aluminum particles bind together through sintering or coalescence at the propellant surface [1], increasing their initial size when they melt to form a droplet before burning. The process is named agglomeration. Figure 1 is a schematic of a solid propellant combustion with aluminum agglomeration on its surface. The increased size due to agglomeration has several effects on both performances and instabilities of Solid Rocket Motor [2–4].
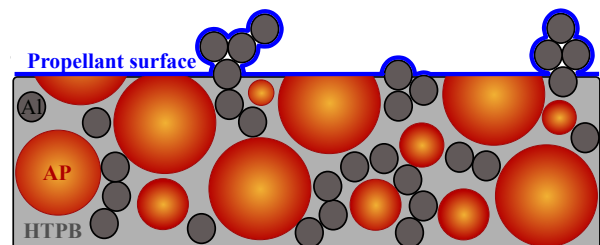

Figure 1: Schematic of a solid propellant combustion with aluminum agglomeration on its surface.

Agglomeration prediction in terms of agglomerate

---
*Corresponding author, Tel.:+33 1 80386230
Email address: thomas.decker@onera.fr (Thomas Geoffrey Decker)

size and agglomeration proportion has been the focus of studies for many decades. Residue and droplet collection after combustion is the basic method used, the data obtained are experimental references [5–8]. Even so, this method is quite demanding and expensive, requiring new tests for new composition or new operation conditions. Correlations based on experimental studies have been established [9–12] but are inappropriate when the studied propellant differs too much from the reference. Some correlations have been established based on pocket models, i.e. with a geometric description of space between AP particles [13–15] but do not consider the effect of pressure on the burning rate. Some numerical models have also been developed, the first are based on random numerical packings [16, 17] but only consider geometry. Some models include both geometric and pressure effects [18–20], considering the ignition phase of the aluminum aggregates, but contain limited agglomeration modeling.

Overall, previous studies have not been able to describe and quantify the physical phenomena at the root of aluminum agglomeration. Experimental studies are still mandatory to investigate agglomeration, with two purposes. The first is to quantify the increase of the size of the droplets due to agglomeration, providing experimental references. The second is to better understand the physics implied in the agglomeration process. Digital Inline Holography (DIH) [21, 22] and shadowgraphy [23] provide image series that can be studied with advanced image analysis tools. The burning surface of the propellant can be analyzed to study agglomeration [24].

The present study is incorporated within the framework of agglomeration physical modelling on the surface of a solid propellant. The modelling needs high-speed experiment data of burning solid propellants to be able to track agglomerates over their lifetime before entering the gas flow. Exploiting the experimental data requires an automatic analysis of the burning surface and detecting the agglomeration patterns. A new multiscale method based on curvature has been developed in order to detect particles and aggregates as a whole and not only a fraction of it.

The method is performed on shadowgraphy images of burning solid propellant containing a low amount of inert particles in order to demonstrate it on well-controlled cases. The solid propellant choice was driven by their relatively low agglomeration (aggregates are usually formed of 2-3 particles). They are therefore simpler to study as a first investigation and are well adapted to develop and adjust the detection method, before applying the method to real propellants.

2. Experimental data

2.1. Shadowgraphy images

Shadowgraphy was used to provide accurate details around the solid propellant surface during combustion, the focusing shadowgraphy set-up used at ONERA was originally made to study aluminum combustion [25]. The shadowgraphy set-up is presented in figure 2. A high-speed camera is used to acquire frames enabling the visualization of the regression of the solid propellant surface. The camera frame-rate is $7500Hz$, the images recorded are 1280 pixels in width and 800 pixels in height. With a spatial resolution of $3\mu m$/pixel, the image real size is approximately 3.8 by 2.4mm.
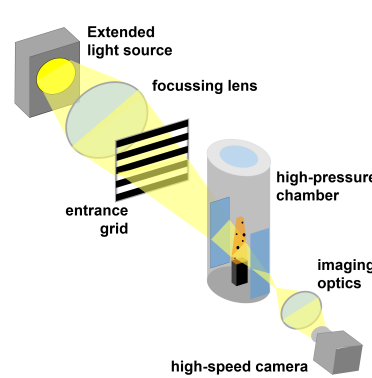

Figure 2: Shadowgraphy set-up [23]

Each frame is divided into two parts, the propellant and the gas flow, the surface of the propellant being the boundary. This frontier is the focus of the study. The first step is to automatically acquire its location, this step has been studied in previous works [26]. The most efficient surface detection method was found to be the Chan-Vese active contour approach [27]. An example of a shadowgraphy image is presented in figure 3. The surface detected by the Chan-Vese active contour is colored in white. The surface is a curve on a 2D plan, it is composed of a finite number of positions along a curvilinear abscissa.

Four solid propellant compositions are studied here. They all contain inert particles instead of aluminum particles. Inert particles do not produce smoke and remain solid at the surface. Aggregates are consequently more easily observed and automatically detected. All four propellant contain HTPB as the binder, a trimodal AP distribution as oxidizing particles and approximately 6% mass fraction of inert particles. The amount of binder and oxidizing particles remain similar from one propellant to another. Three propellants contain ceramic
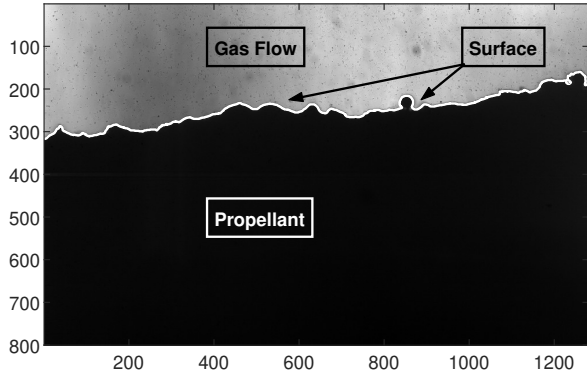
Figure 3: Example of a shadowgraphy frame, with the burning propellant in dark and the gas flow in light color, the surface representation is added in white. Scale in pixels.

particles composed of a ZrO_2, SiO_2 and Al_2O_3 mixture, the fourth contains titanium. The distribution of the inert particles used in the different propellant are summarized in table 1. The representative size of each distribution is the mean particle size D_{10}. The main mode of the inert particles used is between 34 and 90 micrometers.

Each propellant is burnt under pure nitrogen atmosphere at atmospheric pressure. Because the number of frames recorded for each fire-shot at this pressure is very important (around 10000), only one test is studied here for each propellant.

In order to provide a ground truth for the position of agglomeration patterns on the surface and to evaluate detection performances of the new algorithm, annotations have been realized. Annotations have been realized on images chosen regularly all over the test duration in order to annotate different combustion conditions. The total number of images annotated per propellant studied varies from 100 to 115. An example of annotated image of the 2427 propellant is presented in figure 4. The limits of the annotated aggregates are delimited with magenta crosses. The image is trimmed for better visualization.
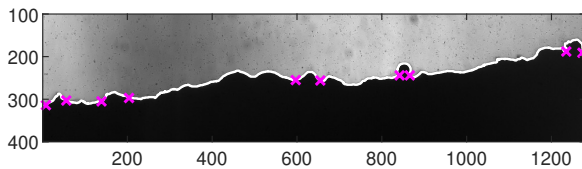

Figure 4: Example of annotated image of the 2427 propellant. The surface is delimited in white and the aggregates annotated are represented with magenta crosses.

2.2. Synthetic images

The new algorithms developed were first applied on a simplified synthetic image for validation purpose. It is made of three protrusions. Each protrusion represents a particle half released from the surface and is different from the others only by its size. The synthetic image is 290 pixels wide and 60 pixels high.

The synthetic image is presented in figure 5, the surface detection using a simple thresholding is presented as well. The objective is to detect all three protrusions and correctly find their limits represented by the red lines.
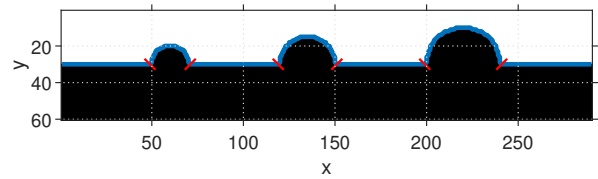

Figure 5: Synthetic image of three half-spheres of different radius with their theoretical limits represented in red, the associated surface detection is represented in blue.

3. Automatic detections of objects on the surface

The goal of the detection algorithm is to isolate patterns of interest from the curve defining the solid propellant surface. The targeted patterns are protrusions associated to emerging particles and aggregates. Aggregates are usually formed of very few particles, rarely exceeding 3. Only the aggregates from the 2430 propellant are sometimes formed of more particles, because the initial particles are smaller. The goal of the presented detection method is to detect particles and aggregates that protrude significantly above the solid propellant burning surface. The method is first applied on the synthetic image for comprehensive purposes. The detection on real shadowgraphy images is presented in the result section 4.

3.1. Surface description

The surface of the propellant is a curve with concave and convex portions. A protrusion is characterize with a concave portion with sufficient size and protuberance, i.e. the upper part of the particle or aggregate emerging from the surface. The protrusion is limited by convex portions, i.e. the link between the particle or aggregate to the propellant. Describing the surface as concave and convex portions is necessary in order to detect and isolate the targeted patterns.

3

Table 1: Particle mass fraction of each studied propellant. The diameter shown is the mean particle size D_{10}.

Particles Propellant	Ceramic			Titanium
	$13\mu m$	$34\mu m$	$90\mu m$	$62\mu m$
2427	0.15	0	6	0
2429	0.13	0.43	5	0
2430	0	6	0	0
2462	0	0	0	6.47

3.1.1. Existing surface description

In previous works [23], the targeted patterns detection and isolation was based on the Curvature Scale Space (CSS) [28]. Unfortunately, the CSS is a description originally used to extract dominating points of a curve for matching [28] or recognition [29], detections are possible but limited to sharp corners [30]. In particular, the CSS only focuses on zero values of curvature while the protrusion detection requires the study of curvature extremums (both maximums and minimums).

Many studies [31–36] proposed adapted CSS focusing more on curvature. They are summarized in table 2. More adaptations are presented in a review by Berreda et al. [37].

Table 2: Different methods from the literature adapted from the CSS.

Method	Description added from the CSS (figure shape)
Extended Curvature Scale Space (Extended CSS) [31]	The classification of convex or concave segments of the curve (2D plot)
Concavity-Convexity Scale Space (CCSS) [32]	Maximums and minimums of curvature are plotted in place of the zeros of curvature (2D plot)
Extreme curvature Scale Space (Extreme CSS) [33]	Extrema of curvature are plotted, and values of curvature are written (2D plot)
Multi-scale Convexity Concavity (MCC) [34, 35]	The displacement of the contour between two scale levels are plotted (2D scalar field)
Curvature Scale Space Transform [36]	Curvatures are directly calculated for all filter widths and are plotted (2D scalar field).

Similarly to the CSS, those descriptors have shape matching and recognition purposes, they are insufficient for protrusion detection. A new description is developed here, the result is a 1D plot highlighting extreme curvatures, their study being necessary and sufficient for protrusion detection.

3.1.2. Extreme of Normalized Curvature (ENC)

We here present our method based on the extreme of normalized curvature concept. Let t be the position on the curve along the curvilinear abscissa, $x(t)$ and $y(t)$ are the functions representing the curve in the space of the frame, $x(t)$ being the abscissa and $y(t)$ the ordinate. t, x and y unit is the pixel.

The curvature κ is obtained by equation 1.

$$\kappa(t) = \frac{\dot{x}\ddot{y} - \dot{y}\ddot{x}}{(\dot{x}^2 + \dot{y}^2)^{\frac{3}{2}}} \tag{1}$$

With $\dot{x} = \frac{\partial x}{\partial t}$, $\ddot{x} = \frac{\partial^2 x}{\partial t^2}$. In order to isolate pattern with various representative scales, the curvature κ must evolve depending on a representative scale. The Gaussian filter $g(t, \sigma) = \frac{1}{\sigma\sqrt{2\pi}} \exp(\frac{t^2}{2\sigma^2})$ is applied to $x(t)$ and $y(t)$ through products of convolution $\circledast$. σ (in pixels) is the Gaussian filter width, the representative scale of the filtering. The result is the abscissa X and the ordinate Y of the curve filtered :

$$\begin{cases} X(t, \sigma) = x(t) \circledast g(t, \sigma) \\ Y(t, \sigma) = y(t) \circledast g(t, \sigma) \end{cases} \tag{2}$$

Curvature is first calculated with no filtering and written κ_0 ($X(t, 0) = x(t), Y(t, 0) = y(t)$). It is then calculated for increasing filtering levels (i.e., increasing filter widths σ). On a frame, the curvature is negative on a convex part and positive on a concave part, because of the orientation of the y-axis pointing downwards (a usual rule in image processing tools). We have chosen to keep this convention, a negative curvature is associated to a convex portion and a positive curvature to a concave portion.

The curve to analyze is presented in figure 6a, the curve being the surface of the synthetic image presented in figure 5. The curve's curvatures $\kappa(t, \sigma)$ using different filter sizes are presented in figure 6b. In compliance with convention, concave portions of the curve result in positive curvatures while convex portions result in negative curvatures.

The surface filtering smooths the surface and hides the effects of small irregularities of the initial surface,
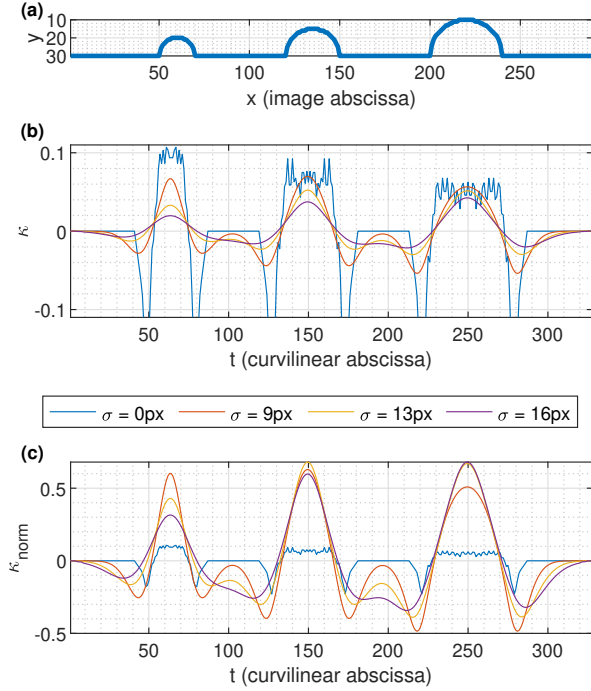
Figure 6: (a) Curve to analyze, (b) Curve's curvatures using different Gaussian filter widths (in pixels). (c) Curve's normalized curvatures using different Gaussian filter widths.

such as protruding AP particles.

The filtering scale σ is an indication of the concavity/convexity scale. But Gaussian filtering mechanically reduces curvature value with increasing σ. A normalization is here added in order to compare curvatures calculated with different filter widths σ. The curvature κ is multiplied by the filter width σ, resulting in the normalized curvature $\kappa_{norm}(t, \sigma) = \sigma\kappa(t, \sigma)$. A matrix $\kappa_{norm}(t, \sigma)$ is calculated from 0 to σ_{max}, for all the t values along the surface. The normalized curvatures $\kappa_{norm}(t, \sigma)$ using four filter sizes between 0 and 16 pixels are presented in figure 6c. The normalized curvature is maximized with a filter width σ depending directly on the size of the protrusion. $\kappa_{norm}(t, \sigma)$ is maximum for $\sigma = 9$ pixels for the smallest protrusion whereas it is maximum for $\sigma = 16$ pixels for the largest.

In order to follow a direct protrusion detection approach, a single plot (function of t) is created from the normalized curvature matrix, by comparing normalized curvature for all filter widths σ. The single plot is a descriptor of the curve. It only keeps the extreme one, either positive or negative:

- $\kappa_{norm} > 0$ represents a concave portion of the curve.
- $\kappa_{norm} < 0$ represents a convex portion of the curve.

The new descriptor is named the Extreme of Normalized Curvature (ENC). For each position t, the ENC calculation returns the extreme curvature value and the associated filter-width $\sigma_{ext}(t)$, giving information on the size of the concavity or the convexity:

$$ENC(t) = \underset{\forall \sigma}{extreme}(\kappa_{norm}(t, \sigma)) \qquad (3)$$

$$\sigma_{ext}(t) = \sigma \mid \kappa_{norm}(t, \sigma) = ENC(t) \qquad (4)$$

ENC displays either the concavity (when positive) or convexity (when negative) of the curve. It compares the normalized curvature of the filtered curve using different filter width σ. The more extreme the ENC is, the more concave/convex the curve is. $\sigma_{ext}(t)$ is the filter width associated to $ENC(t)$, i.e. the filter width for which the curve is the more concave or convex. At this point, we would like to stress that ENC is defined as the extreme value of normalized curvature among all filter widths, and not the extreme value of curvature, as given by equation 1.

The ENC plot for the synthetic image is presented in figure 7a, the filter width associated $\sigma_{ext}(t)$ is presented in figure 7b. The maximums of ENC correspond to the center of the concavities of the curve. The minimums of ENC are located at the protrusion limits (convex parts). Using directly the ENC to search for the limits of the protrusions is only possible for synthetic images such as the one studied, not real images. The reason is that the surface is not plane as in the synthetic image. The convex portions delimiting the protrusions are not as sharp as in the synthetic image, resulting in minimums of curvature sometimes wrongly placed.

As an example, ENC for a real shadowgraphy image is shown in figure 8a. ENC clearly increased the concave portions and facilitate protrusion detection. The image is trimmed and positions are regularly represented by cyan crosses in figure 8b in order to link the surface to the ENC.

3.2. Method

The automatic detection and isolation can not only be realized by ENC because the convexities are sometimes wrongly placed. Furthermore, representative size and protuberance of the protrusions must be calculated in order to detect only the patterns with sufficient size and protuberance.

The automatic detection and isolation is realized in two parts. The first is the protrusion presence detection, i.e. the detection of concave portions of the curve with sufficient size and protuberance. The protrusion presence detection is realized in four steps and presented in
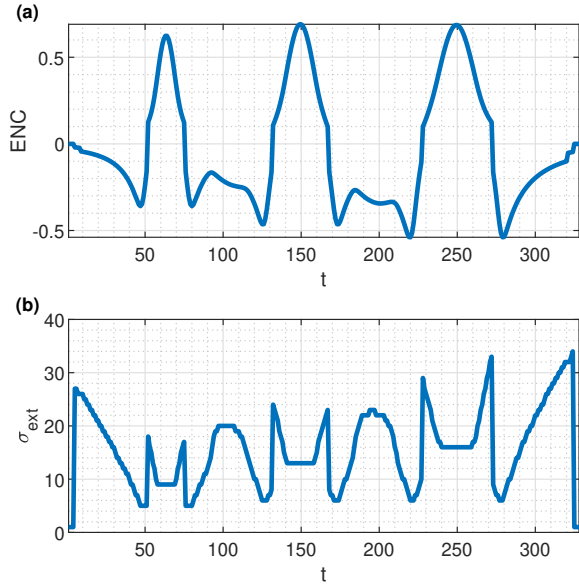
5

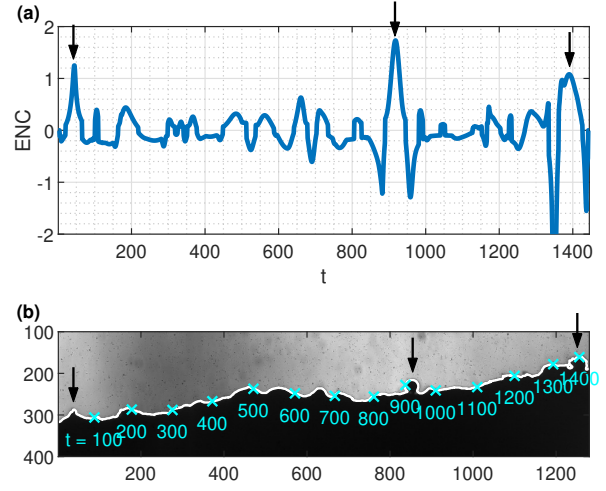Figure 7: (a) ENC plot, (b) Filter width associated $\sigma_{ext}(t)$ plot, both of the synthetic image.

Figure 8: (a) ENC of the surface of the propellant studied, (b) Trimmed image with the surface studied represented in white. Positions are regularly represented by cyan crosses. Arrows indicate the location of three specific patterns.

section 3.2.1. The second is protrusion limit research, i.e. the research of the convex portions of the curve around the convex portion. The protrusion limit research is realized in two steps and presented in section 3.2.2.

3.2.1. Protrusion presence detection

Step 1 : concave portions detection

A protrusion on the surface of the propellant is a concavity to detect with positive curvatures. Therefore, detecting protrusions is obtained by detecting the ENC maximums. Examples of convexities represented with ENC local maximums are located at $t \approx 900$ pixels and $t \approx 1400$ pixels in figure 8. All local maximums with prominence equals or superior to a parameter *MinProminence* are detected. The prominence is the ENC difference between the local maximum and its surrounding local minimums.

The parameter *MinProminence* is chosen low, i.e. 0.3 here (in ENC units), in order to miss as few protrusions as possible. Protrusion detections are then validated with other criteria, i.e. the filter width and the curvature associated to the protrusion. They are calculated as follows.

Step 2 : representative size calculation

From the step 2, each detection is studied separately. The presentation of the different steps is realized on the second protrusion with intermediate size from figure 5.

Let t_i the location of the ENC maximum associated to detection #i. Let $t_i(1)$ and $t_i(2)$ be the left and right borders delimiting the concave portion of the curve associated to detection #i. They are the zero values of ENC closest to t_i. The filter width associated to the detection $\overline{\sigma_i}$ is calculated as the mean of the filter width associated to the ENC $\sigma_{ext}(t)$ on the interval $[\![t_i(1) ; t_i(2)]\!]$. $\overline{\sigma_i}$ is the mean filter width on the concave portion of the curve, it is the representative size of the protrusion. Averaging the filter width aims at reducing sensitivity to a local value of curvature, therefore considering the whole concavity of the protrusion and not only its maximum.

The mean filter $\overline{\sigma_i}$ calculated for the second protrusion is $\overline{\sigma_2} = 14$ pixels (mean value calculated between the two vertical dashed lines representing $t_2(1)$ and $t_2(2)$ in figure 9).

Step 3 : representative protuberance calculation

A normalized curvature value κ_i is calculated for each detection #i. It is the maximum normalized curvature value κ_{norm} for the scale representative of the studied protrusion, e.g. $\overline{\sigma_i}$. $\kappa_{norm}(\overline{\sigma_i})$ is shown in figure 10, where κ_i corresponds to the asterisk at the top of the curve.
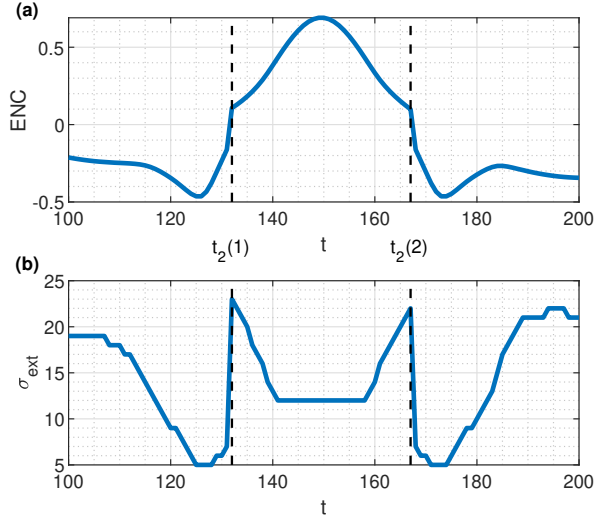
6

Figure 9: (a) ENC positive borders research. (b) Mean filter calculation, for detection #2 of the synthetic image.
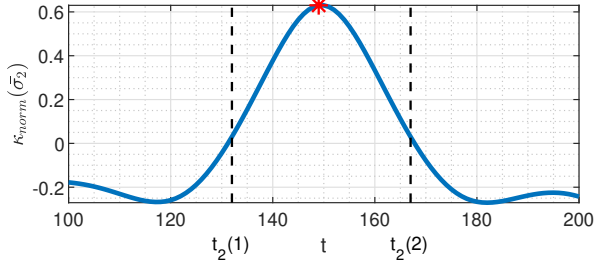

Figure 10: Calculation of the maximum of normalized curvature, for detection #2 of the synthetic image.

The filter width $\overline{\sigma_i}$ is related to the size of the protrusion while its normalized curvature κ_i represents its protuberance from the surface, i.e. how a protrusion surpasses the propellant surface.

Step 4 : validation of the detection

The two features $\overline{\sigma_i}$ and κ_i of each detection #i determine whether it is a valid protrusion or not. Two thresholds $\overline{\sigma}_{min}$ and κ_{min} are used. The detection #i is validated if $\overline{\sigma_i} > \overline{\sigma}_{min}$ and $\kappa_i > \kappa_{min}$. The thresholds $\overline{\sigma}_{min}$ and κ_{min} are determined using the annotations. They are chosen in order to maximize the detection performances, the process will be presented in section 4.1.

The thresholding of the two features $\overline{\sigma_i}$ and κ_i leads to the detection of patterns whose representative size ($\overline{\sigma_i}$) and protrusion (κ_i) are sufficiently large and represen-

tative of real agglomeration patterns associated to the inert particles. This aims at avoiding detecting all the surface irregularities such as protruding AP particles.

3.2.2. Protrusion limits research

Step 5 : temporary limits research

The limits of the protrusion are the convexities of the curve, linking the particle or aggregate to the propellant surface. Because an aggregate is formed of several particles, there may be convexities within the inner portions of the protrusion and not only on its limits.

The research of the protrusions limits is performed in two steps in order to be more robust. The first is the research of temporary limits using the mean filter $\overline{\sigma_i}$ associated to the detection. The mean filter $\overline{\sigma_i}$ is related to the real size of the protrusion, enabling the detection of the total of an aggregate and not only a fraction of it. Then a refinement of the temporary limits is realized using the curvature without filtering κ_0, because it corresponds to the real protrusion with all its details.

The left and right temporary limits $\overline{t_i}(1)$ and $\overline{t_i}(2)$ are calculated using the position t_i of the detection and the associated filter width $\overline{\sigma_i}$. They are the nearest left and right local minimums of the normalized curvature $\kappa_{norm}(\overline{\sigma_i}, t)$ to the detection position t_i. The temporary limits research is illustrated in figure 11a, where it is applied on the second protrusion of the synthetic image. The red asterisk is the location of the maximum κ_i, the green asterisks are the temporary limits of the protrusion.

Step 6 : final limits research

The temporary limits $\overline{t_i}(1)$ and $\overline{t_i}(2)$ are convexities of the filtered curve. The final limits must be convexities of the unfiltered curve. The final limits $\tilde{t}_i(1)$ and $\tilde{t}_i(2)$ are chosen from the unfiltered curvature κ_0 as the closest local minimums of κ_0 to the temporary positions $\overline{t_i}(1)$ and $\overline{t_i}(2)$. The final limits research is the final step of the method. It is illustrated in figure 11b on the second protrusion of the synthetic image. The green asterisks are the temporary limit, the black asterisks are the final limits of the protrusion.

3.3. Summary of the method

The detection of the particles and aggregates and the research of their limits is realized in six steps, they are summarized in table 3.

Figure 12 is the synthetic image studied with the three protrusions detected plotted in different colors. The
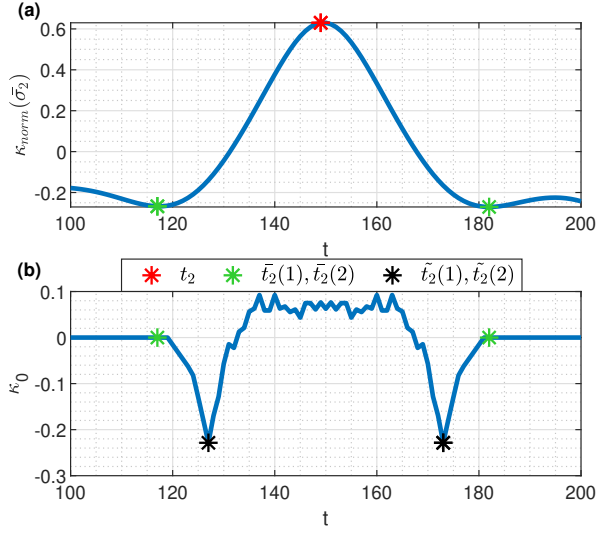
Figure 11: (a) Temporary limits (green asterisk) research (b) Final limits (black asterisk) research, for detection #2 of the synthetic image.

Table 3: The six steps to obtain the protrusions from the surface curve.

Step	Results
1. ENC creation and detection of maximums	ENC and $\{ t_i \mid i \in [\![1 \, ; \, N]\!] \}$
For each detection $i = 1 : N$	
2. ENC positive borders research and mean filter calculation	$t_i(1)$, $t_i(2)$ and $\overline{\sigma}_i$
3. Maximum of normalized curvature calculation	κ_i
4. Validation of the detection	
If validation	
5. Temporary limits research	$\overline{t}_i(1)$ and $\overline{t}_i(2)$
6. Final limits research	$\tilde{t}_i(1)$ and $\tilde{t}_i(2)$

method correctly detects the protrusions, their limits are correctly placed, confirming the necessity to research the protrusions limits by a two-step method.
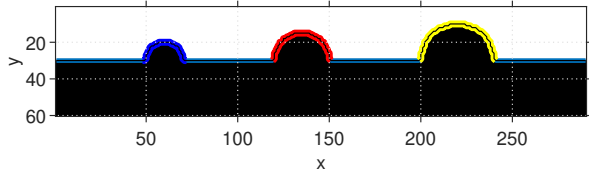

Figure 12: Synthetic image with the protrusions plotted with different colors, obtained with our algorithm.

4. Performances

On real images, objects of interest are protrusions with sufficient size and protuberance. The algorithm separate those protrusions from all the protrusions detected thanks to the thresholding of the two features $\overline{\sigma}_i$ and κ_i during the step 4 (validation of the detections) of the method. The values of the parameters $\overline{\sigma}_{min}$ and κ_{min} are chosen in order to optimize the detection performances.

4.1. Protrusion presence detection

The annotations enable the performance calculation of the protrusion presence detection through a

classification. The comparison between detections and annotations are realized with the positions of the maximums detected on the ENC and the annotated limits of the protrusions (represented by magenta crosses in figure 4). The purpose of the annotations process is to select the two parameters of the detection method, the two features $\overline{\sigma}_{min}$ and κ_{min}. By maximizing the global score of detection, the detection method aligns as closely as possible to the annotations, the latter representing what should be detected (i.e. inert particles).

The protrusions are classified in three categories :
- True Positive (TP) when the position of a maximum t_i is included between the limits of an annotation, the detection is confirmed by an annotation. Each annotation can confirm only one detection.
- False Positive (FP) otherwise.
- False Negative (FN) when an annotation does not confirm any detection

Two performances metrics are calculated :
- The precision $Pr = \frac{TP}{TP+FP}$.
- The recall $Re = \frac{TP}{TP+FN}$.

Precision quantifies the proportion of false detections. Recall is used to verify that all annotation are indeed detected. When more protrusions are detected by decreasing the two parameters $\overline{\sigma}_{min}$ and κ_{min}, the precision decreases while the recall increases. A compromise is necessary, the F_1 score is usually used in image processing. It takes into account both performances metrics

8

following equation 5.

$$F_1 = 2\frac{Pr.Re}{Pr + Re} \tag{5}$$

The objective is to maximize the F_1 score by choosing the appropriate parameters $\overline{\sigma}_{min}$ and κ_{min}.

In order to adjust the two threshold values, a detection without thresholding is realized in order to detect all real protrusions and many false protrusions. All protrusions detected are kept and the associated features $\overline{\sigma}_i$ and κ_i are calculated. The detections are compared to the annotations and classified as TP or FP. Figure 13 is a scatter plot with the parameters $\overline{\sigma}_i$ and κ_i of the detections as the graph axes. Each cross/point is a detection, its color representing whether it is confirmed by an annotation (classified as TP) or not (classified as FP). The propellant studied is the 2427 propellant.
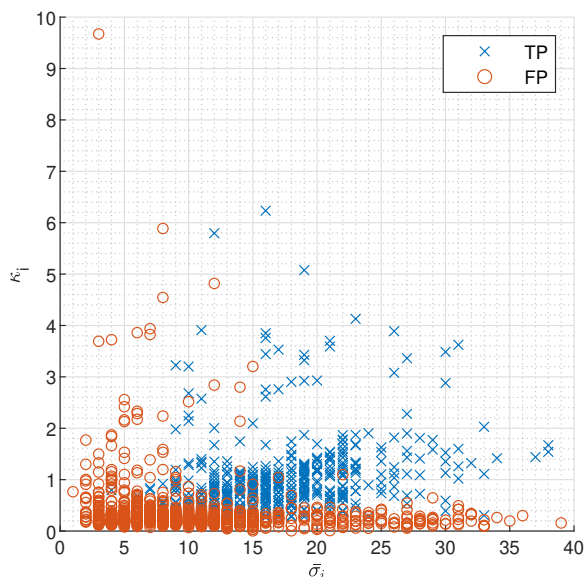

Figure 13: Classification of the detections depending on the parameters $\overline{\sigma}_i$ and κ_i (propellant 2427).

A first observation is that the top-right part of the plot is mostly filled with TP and the bottom-left part with FP. This was anticipated because a detection with high $\overline{\sigma}_i$ and κ_i is a big protrusion, likely to be annotated.

The parameters $\overline{\sigma}_{min}$ and κ_{min} must be chosen in order to maximize the F_1 score. Figure 14 is a 2D surface plot representing the F_1 score depending on the parameters $\overline{\sigma}_{min}$ and κ_{min} chosen for the thresholding.

The parameter $\overline{\sigma}_{min}$ appears to have less influence, a huge zone from $\overline{\sigma}_{min} = 6$ to $\overline{\sigma}_{min} = 10$ pixels has F_1
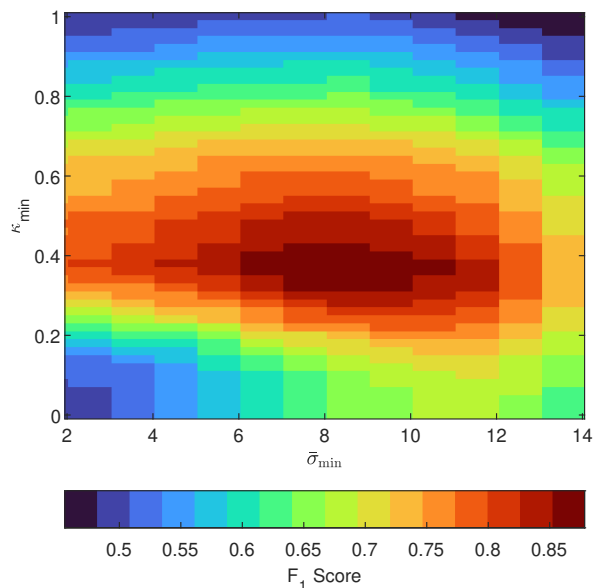

Figure 14: Surface plot of the F_1 score depending in the two parameters $\overline{\sigma}_{min}$ and κ_{min} (propellant 2427).

score of at least 0.85. The parameter κ_{min} seems to directly influence the F_1 score. This observation is confirmed by figure 15, it is a Precision-Recall curve with a κ_{min} from 0.3 to 0.5 with a 0.02 increment. The parameter $\overline{\sigma}_{min}$ is set to 8 pixels. The F_1 score isolines are drawn in black.

The performances are good for the whole range of κ_{min} considered, Recall and Precision are always superior to ≈ 0.80. A small variation of the parameter κ_{min} does not significantly change the performances. The F_1 score varies slightly from 0.82 to 0.87. The performances (Precision and Recall) and the F_1 score for three values of κ_{min} (minimum, optimum and maximum) are shown in table 4. A κ_{min} of 0.38 maximizes the F_1 score

Table 4: Performances for the minimum and maximum of κ_{min} (propellant 2427).

κ_{min}	Precision	Recall	F_1 score
0.30 (Min)	0.79	0.90	0.84
0.38 (Opt)	0.88	0.86	0.87
0.50 (Max)	0.93	0.74	0.82

The maximum F_1 score is obtained with a parameter κ_{min} equal to 0.38, with precision and recall very close. Figure 16 is the real image of the 2427 propellant presented in figure 3 with the detected protrusions plotted in different colors. The two parameters $\overline{\sigma}_{min}$ and
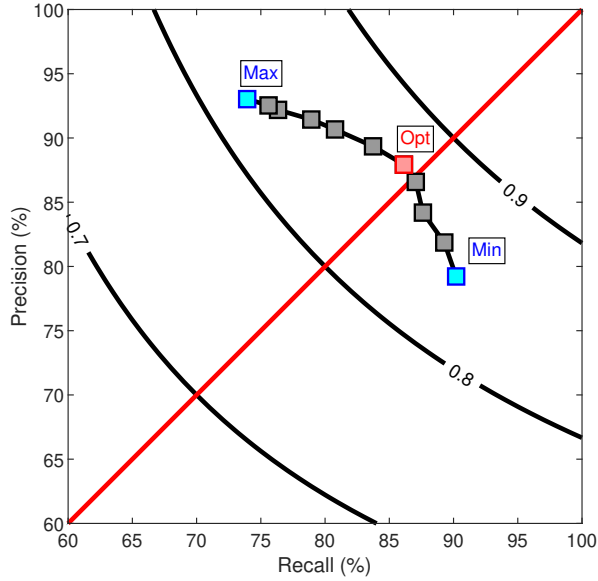
Figure 15: PR-curve depending on the parameter κ_{min} ($0.3 \leq \kappa_{min} \leq 0.5$). The parameter $\overline{\sigma}_{min}$ is set to 8 pixels (propellant 2427).

κ_{min} chosen are the optimum parameters calculated. The presence of the five protrusions annotated (visible in figure 2) have been correctly detected. Figure 17 is the detection of an image with a coral-like aggregate on the surface (see the left dark blue structure), showing the ability of the method to detect complex-shaped patterns. Figure 17a is the captured image, figure 17b is the image with the detected protrusions plotted in different colors.
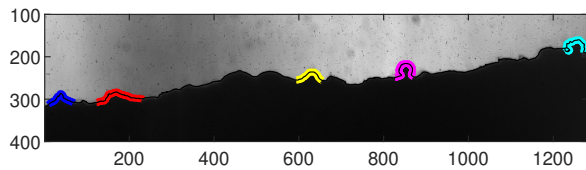

Figure 16: Real image with the protrusions plotted with different colors (propellant 2427).

The influence of the parameter κ_{min} is similar for all propellants. Large κ_{min} involves high precision but low recall. The parameter κ_{min} maximizing the F_1 score differs slightly from one propellant to another (from 0.38 to 0.57). The performances and the maximized F_1 score are presented in table 5 for the four propellants, with κ_{min} for each of them. The parameter $\overline{\sigma}_{min}$ is set to 8 pixels for all propellants. For all propellants, the optimum parameters $\overline{\sigma}_{min}$ are really close to 8 pixels and a small
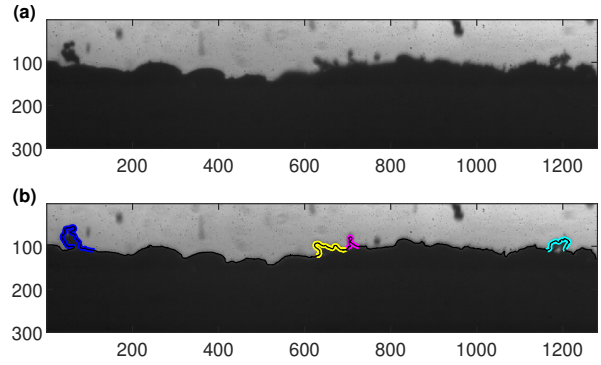

Figure 17: (a) Real image (b) Real image with the protrusions plotted with different colors (propellant 2430).

variation of it marginally changes the performances.

Table 5: Detection performances with a κ_{min} maximizing the F_1 score for all propellants studied ($\overline{\sigma}_{min} = 8$ pixels).

Propellant	κ_{min}	Precision	Recall	F_1 score
2427	0.38	0.88	0.86	0.87
2429	0.47	0.93	0.94	0.88
2430	0.58	0.90	0.90	0.90
2462	0.57	0.81	0.85	0.83

Overall, detection performances for agglomeration patterns are good. The F_1 score varies from 0.83 to 0.90. For each propellant studied, both precision and recall are above 80%.

The annotation process itself is slightly uncertain. Some of the present false detections correspond to shallow protrusions associated to single particle, that could have been annotated. Precision might then be slightly underestimated. Similarly, some of the missed annotations (i.e. FN) are protrusions from single particles only partially above from the surface, that are not the main target for agglomeration study.

The parameter κ_{min} maximizing the F_1 score does seem to be linked to the particles initial size of the propellants studied. The parameter is smaller for the 2427 and 2429 propellants than for the 2430 and 2462 propellants, i.e. for compositions with larger particles.

4.2. Image selection sensitivity

The previous analysis might be biased by the sets of annotated images that were used for performance estimation. In order to investigate the sensitivity of the performance estimation, performances were estimated for random sets of annotated images.

A random sub-sampling was tested on the 111 annotated images for composition 2427. Half the annotated images are picked randomly (55 images) and performances are evaluated by comparing the detections of the algorithm and the annotations on those randomly picked images only.

The performances are presented in figure 18. The four colored plots show the performances of the four arbitrary samplings. The black curve is the original plot presented in figure 15, representing the performances calculated for the complete 111 annotated image set.
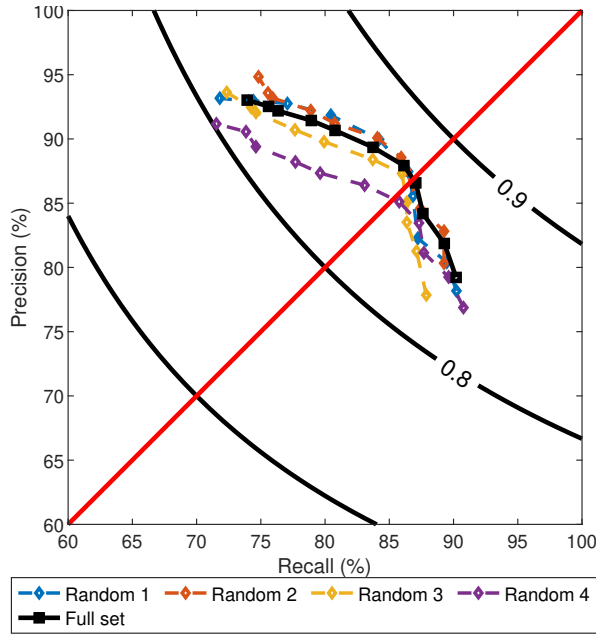

Figure 18: Performance plots depending on the parameter κ_{min} for random samplings of the whole annotated image set (propellant 2427).

The performances are really close from one sampling to another. With the same parameter κ_{min}, the highest relative error between the F_1 score of two random sampling is equal to 2.61%. The optimum parameter κ_{min} is equal to 0.38 for three out of the four random sampling, and is equal to 0.40 for the last one. Hence estimating the optimum value for κ_{min} does not depend on the selected annotated images, provided it includes enough targeted patterns, i.e. several hundreds.

4.3. Limits research

The limits research is the second part of the automatic detection and isolation of protrusions. Delimiting the protrusion is as important as detecting their presence, in order to correctly place the protrusions on the surface of the propellant. Performances are evaluated by comparing the researched limits to the annotated limits (magenta crosses in figure 4). The comparison is realized by comparing the size of the protrusion detected by the algorithm to the protrusion annotated.

The size of the protrusion is related to its limits. If the final limits found by the algorithm are too distant to the position t_i, the size of the protrusion detected is too large. On the contrary, if the final limits are too close to t_i, the size of the protrusion detected is too low.

For each detection classified as TP, pattern area is estimated, delimited on the bottom part by the segment connecting the two pattern borders. For both detection and annotation areas, the equivalent diameter is calculated considering an aggregate as a disk following equation 6.

$$D_{eq} = 2\sqrt{\frac{Area}{\pi}} \tag{6}$$

Figure 19 is a scatter plot with each dot being a protrusion of the TP category. The x-axis and the y-axis are respectively the equivalent diameter for annotations and detections. The figure is divided into six different areas, depending on the ratio between $D_{eq}(detection)$ and $D_{eq}(annotation)$. The dashed lines represent a ±10% tolerance interval and the dotted lines a ±25% tolerance interval. The full line is $D_{eq}(detection) = D_{eq}(annotation)$.
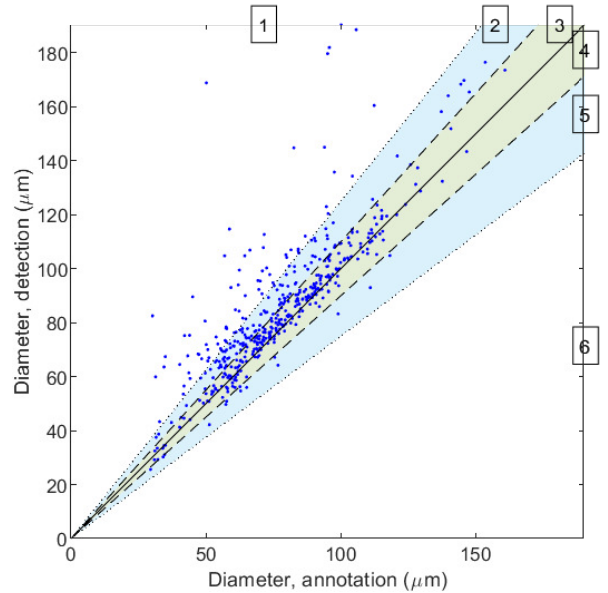

Figure 19: Scatter plot of the comparison between annotated and detected protrusions equivalent diameters (propellant 2427).

The percentage of protrusions in the different areas

are shown in table 6. Around 84% of the protrusions are within the ±25% tolerance. An overestimation of the size of the detections can be noticed, that seems attributed to the estimation of the mean filter $\overline{\sigma_i}$. The mean filter $\overline{\sigma_i}$ is always superior to the filter width $\sigma_{ext}(t)$ located at the maximum of ENC t_i. The trend is similar for all propellants, around 80% of the protrusions are within the ±25% tolerance with the 20% left being oversized.

The overestimation of the mean filter $\overline{\sigma_i}$ admittedly leads to larger protrusions detected but prevents the detection of sub-parts of a protrusion. This would be the case if a protrusion is made of an aggregation of spherical particles.

Detecting sub-parts of a protrusion would cause uncertainties when trying to associate an aggregate on two successive images. Following a surface pattern over time on successive images is a crucial aspect of agglomeration characterization. It is thus preferable to overestimate the detections than detecting sub-parts of the protrusions.

Table 6: Proportion of detection in each class for equivalent diameter relative to annotation diameter (propellant 2427).

Area	$\frac{D_{eq}(detection)}{D_{eq}(annotation)}$ interval	Proportion
1	> 1.25	16%
2	1.1 − 1.25	23%
3	1.0 − 1.1	43%
4	0.9 − 1.0	15%
5	0.75 − 0.9	3%
6	< 0.75	0%

5. Limitations and improvements

Shadowgraphy captures a 1D "integrated" surface while the real surface of the propellant is 2D (integration over the depth of field). Due to the image projection, particles and aggregates can be hidden by parts of the solid propellant, or even other particles. The propellant 1D "integrated" surface is irregular, protruding AP particles or binder could be represented by a a soft concave portion on the 1D curve. The whole process of filtering and thresholding of the present detection method aimed at limiting as much as possible wrong detections.

A special attention on the propellant ignition was performed in order to get a burning surface as plane and horizontal as possible, limiting the irregularity of the surface due to other things than particles or aggregates,

such as high curvature levels induced by a portion of the sample ignited before the others. In addition, the sample thickness and the depth of field are relatively small ($1 − 2mm$) to try to reduce the projection effects.

In order to further improve robustness, a coupling with the detections of particles/aggregates in the gas flow is considered. The gas flow is transparent, the detection of inert particles in it gives good results [26]. A first work on this coupling has been published [38]. Figure 20, taken from [38], shows a coupling example. Figure 20a is a detection on the surface with the method presented in this article, figure 20b is the coupled detection in the gas flow on the following image.
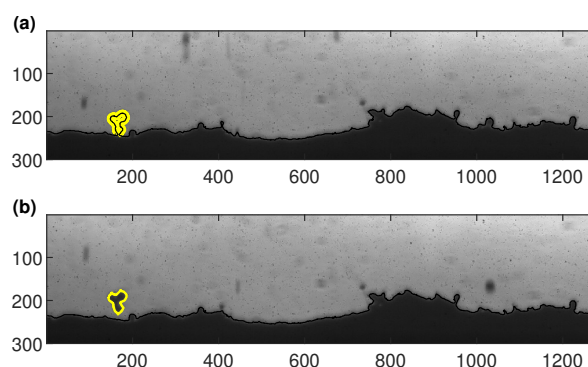

Figure 20: (a) A detection on the surface (b) Coupled detection in the gas flow on the following image.

Surface detections can be followed easily over time [38] and their ejection in the gas flow is either confirmed or invalidated. The coupling with the detections in the gas flow aims at making the surface detection method more robust, thus allowing to solve (at least partially) the problems raised previously by limiting the amount of wrong detection.

Sizes of particles and aggregates in the gas flow can be estimated with good precision [26]. The unagglomerated particles size should be very similar to the initial particles, comparing the two size distributions is a way to examine the correct application of the detection method. Furthermore, the relevance of the approach can be checked by comparing the detected sizes (of particles and aggregates) with standard collection techniques (e.g. quench bombs) in future works.

6. Conclusions

An algorithm detecting particles and aggregates on the surface of a solid propellant has been developed. A new descriptor, the Extreme of Normalized Curvature

(ENC) has been created based on the curvature of the curve using Gaussian filters of different widths. The detection of convex parts, potentially being a particle or an aggregate, is obtained by locating the maximums of the ENC. Two features are calculated for each detection and give information about the size and the protuberance of the detection. A thresholding is performed in order to validate the detections of sufficient size and protuberance. The research of the limits of the detections follows a multi-scale approach.

Detection performances for the algorithm have been evaluated by comparing the detections to manual annotations. A parametric study has been realized in order to find the most suitable parameter to implement in the algorithm. The maximum F_1 score calculated varies from 0.83 to 0.90, depending on the propellant studied. Globally, the algorithm correctly detects particles and aggregates on the solid propellant surface. The optimum parameter determination does not seem to be much sensitive to the set of images annotated.

The research of the limits of the protrusions has also been evaluated by comparing the equivalent diameters of the detections to the annotations. Concerning the 2427 propellant, about 84% of the detections have equivalent diameters relatively close to the annotation, within a ±25% tolerance.

The detection method has some limitations. Experimental efforts reduce the potential of the mentioned limitations. A further consolidation of the surface detection method through the coupling with detections in the gas flow aims at improving robustness and undermine its limitations.

The final stage is to apply the algorithm of detections to propellant containing aluminum particles, those are employed in Solid Rocket Motors. The detection method can detect particles and aggregates before they start to merge. New image processing tools are required in order to detect the merging aggregate when it turns into a droplet.

References

[1] E. W. Price, R. K. Sigman, Combustion of aluminized solid propellants, Solid propellant chemistry, combustion, and motor interior ballistics (Progress in Astronautics and Aeronautics) 185 (2000) 663–687.

[2] M. Salita, Deficiencies and requirements in modeling of slag generation in solid rocket motors, J. Prop. Power 11 (1) (1995) 10–23.

[3] J. Dupays, Two-phase unsteady flow in solid rocket motors, Aerospace Science and Technology 6 (6) (2002) 413–422.

[4] S. Gallier, F. Godfroy, Aluminum combustion driven instabilities in solid rocket motors, J. Prop. Power 25 (2) (2009) 509–521.

[5] P. F. Pokhil, A. F. Belyaev, Y. V. Frolov, V. S. Logachev, A. I. Korotkov, Combustion of metal powders in active media, Defense Technical Information Center, Technical Report AD0769576 (1972).

[6] P. L. Micheli, W. G. Schmidt, Behavior of aluminum in solid rocket motors, Aerojet Solid Propulsion Co (1977).

[7] J. K. Sambamurthi, E. W. Price, R. K. Sigman, Aluminum agglomeration in solid-propellant combustion, AIAA J. 22 (8) (1984) 1132–1138.

[8] V. A. Babuk, Combustion of a metallized fuel within the composition of rocket propellants, in: Intrachamber Processes, Combustion, and Gas Dynamics of Disperse Systems, St. Petersburg (Russia), 1996, pp. 74–85.

[9] M. W. Beckstead, A model for solid propellant combustion, in: 14th JANNAF Combustion Meeting, Baltimore, Maryland (USA), Vol. 1, 1977, pp. 281–306.

[10] R. W. Hermsen, Aluminum combustion efficiency in solid rocket motors, in: AIAA 19th Aerospace Sciences Meeting, 1981.

[11] M. Salita, Survey of recent al2o3 droplet size data in solid rocket chambers, nozzles, and plumes, 31th JANNAF Combustion Meeting, Sunnyvale (USA) (1994).

[12] J. Duterque, Experimental study of the agglomeration of aluminum in solid propellant motors, 4th International Symposium on Special Topics in Chemical Propulsion, Stockholm (Sweden) (1996).

[13] N. S. Cohen, L. D. Strand, A model for the burning rates of composite propellants, in: 17th JANNAF Combustion Meeting, Hampton (USA), Vol. 1, 1980, pp. 53–97.

[14] N. S. Cohen, A pocket model for aluminum agglomeration in composite propellants, AIAA J. 21 (5) (1983) 720–725.

[15] V. G. Grigoriev, K. P. Kutsenogii, V. E. Zarko, Model of aluminum agglomeration during the combustion of a composite propellant, Combustion, Explosion and Shock Waves 17 (4) (1981) 356–363.

[16] T. Jackson, F. Najjar, J. Buckmaster, A new class of agglomeration models for aluminum composite propellants based on random packs, J. Prop. Power 21 (5) (2005) 925.

[17] S. Gallier, A stochastic pocket model for aluminum agglomeration in solid propellants, Propellants, Explosives, Pyrotechnics 34 (2) (2009) 97–105.

[18] V. Srinivas, S. R. Chakravarthy, Computer model of aluminum agglomeration on burning surface of composite solid propellant, J. Prop. Power 23 (4) (2007) 728–736.

[19] M. W. Tanner, Multidimensional modeling of solid propellant burning rates and aluminum agglomeration and one-dimensional modeling of RDX/GAP and AP/HTPB, Ph.D. thesis, Brigham Young University (2008).

[20] M. Plaud, S. Gallier, A numerical mesoscale model for aluminum agglomeration in solid propellants, in: 7th European Conference for Aeronautics and Space Sciences, Milan (Italy), 2017.

[21] Y. Chen, D. R. Guildenbecher, K. N. G. Hoffmeister, M. A. Cooper, H. L. Stauffacher, M. S. Oliver, E. B. Washburn, Study of aluminum particle combustion in solid propellant plumes us-

ing digital in-line holography and imaging pyrometry, Combustion and Flame 182 (2017) 225–237.

[22] M. S. Powell, I. W. Gunduz, W. Shang, J. Chen, S. F. Son, Y. Chen, D. R. Guildenbecher, Agglomerate sizing in aluminized propellants using digital inline holography and traditional diagnostics, J. Prop. Power 34 (4) (2018) 1002–1014.

[23] R. W. Devillers, G. Le Besnerais, M. Nugue, N. Cesco, Experimental analysis of solid-propellant surface during combustion with shadowgraphy images: new tools to assist aluminum-agglomeration modelling, in: 7th European Conference for Aeronautics and Space Sciences, Milan (Italy), 2017.

[24] M. Liu, Z. Liu, S. Li, W. Yu, N. Wang, Characterization of the initial agglomerates of aluminized composite propellants, Acta Astronautica 188 (2021) 130–139.

[25] F. Cauty, C. Erades, Tracking of aluminum particles burning in solid propellant combustion gases by focusing schlieren technique, in: 15th International Symposium on Flow Visualization, Minsk (Belarus), Vol. 9, 2012.

[26] M. Nugue, Outils pour l'étude conjointe par simulation et traitement d'images expérimentales de la combustion de particules d'aluminium utilisées dans les propergols solides, Ph.D. thesis, Paris Saclay (2019).

[27] T. F. Chan, L. A. Vese, Active contours without edges, IEEE Transactions on image processing 10 (2) (2001) 266–277.

[28] F. Mokhtarian, A. Mackworth, Scale-based description and recognition of planar curves and two-dimensional shapes, IEEE transactions on pattern analysis and machine intelligence 1 (1986) 34–43.

[29] F. Mokhtarian, Silhouette-based occluded object recognition through curvature scale space, Machine Vision and Applications 10 (3) (1997) 87–97.

[30] F. Mokhtarian, R. Suomela, Robust image corner detection through curvature scale space, IEEE Transactions on Pattern Analysis and Machine Intelligence 20 (12) (1998) 1376–1381.

[31] S. Kopf, T. Haenselmann, W. Effelsberg, Shape-based posture and gesture recognition in videos, in: Storage and Retrieval Methods and Applications for Multimedia, San Jose, CA (USA), Vol. 5682, SPIE, 2005, pp. 114–124.

[32] A. E. de Luna, C. Miravet, D. Otaduy, C. Dorronsoro, A decision support system for ship identification based on the curvature scale space representation, in: Electro-Optical Remote Sensing, Bruges(Belgium), Vol. 5988, SPIE, 2005, pp. 171–182.

[33] H. Silkan, S. E. Ouatik, A. Lachkar, M. Meknassi, A novel shape descriptor based on extreme curvature scale space map approach for efficient shape similarity retrieval, in: 5th International Conference on Signal Image Technology and Internet Based Systems, Marrakech (Morocco), IEEE, 2009, pp. 160–163.

[34] T. Adamek, N. E. O'Connor, A multiscale representation method for nonrigid shapes with a single closed contour, IEEE Transactions on Circuits and Systems for Video Technology 14 (5) (2004) 742–753.

[35] T. Adamek, N. E. O'connor, N. Murphy, Multi-scale representation and optimal matching of non-rigid shapes, Methods 13 (2005) 14.

[36] G. Cerutti, L. Tougne, D. Coquin, A. Vacavant, Curvature-scale-based contour understanding for leaf margin shape recognition and species identification, in: 8th International Conference on Computer Vision Theory and Applications, Barcelona (Spain), Vol. 1, 2013, pp. 277–284.

[37] F. Berrada, D. Aboutajdine, S. E. Ouatik, A. Lachkar, Review of 2d shape descriptors based on the curvature scale space approach, in: International Conference on Multimedia Computing and Systems, Ouarzazate (Morocco), IEEE, 2011, pp. 1–6.

[38] T. G. Decker, R. W. Devillers, S. Gallier, Agglomeration in solid propellants loaded with inert particles – study of physi-

cal phenomena using shadowgraphy image processing, in: 9th European Conference for Aeronautics and Space Sciences, Lille (France), 2022.